Experimental Evidence of Plasmoids in High-β Magnetic Reconnection

J. A. Pearcy,[1,*] M. J. Rosenberg,[2] T. M. Johnson,[1] G. D. Sutcliffe,[1] B. L. Reichelt,[1] J. D. Hare,[1] N. F. Loureiro,[1] R. D. Petrasso,[1] and C. K. Li[1,†]

[1]*Plasma Science and Fusion Center, Massachusetts Institute of Technology, Cambridge, Massachusetts 02139, USA*
[2]*Laboratory for Laser Energetics, University of Rochester, Rochester, New York 14623, USA*

(Received 8 July 2022; revised 27 October 2023; accepted 7 December 2023; published 18 January 2024)

Magnetic reconnection is a ubiquitous and fundamental process in plasmas by which magnetic fields change their topology and release magnetic energy. Despite decades of research, the physics governing the reconnection process in many parameter regimes remains controversial. Contemporary reconnection theories predict that long, narrow current sheets are susceptible to the tearing instability and split into isolated magnetic islands (or plasmoids), resulting in an enhanced reconnection rate. While several experimental observations of plasmoids in the regime of low-to-intermediate β (where β is the ratio of plasma thermal pressure to magnetic pressure) have been made, there is a relative lack of experimental evidence for plasmoids in the high-β reconnection environments which are typical in many space and astrophysical contexts. Here, we report strong experimental evidence for plasmoid formation in laser-driven high-β reconnection experiments.

DOI: 10.1103/PhysRevLett.132.035101

Magnetic reconnection is the process by which magnetic fields in plasmas change their topologies and release magnetic energy [1,2]. It is a phenomenon with widespread importance to many fields of physics, from astrophysics [1–5] to laboratory and fundamental plasma physics [1–3,6–11]. The theoretical understanding of magnetic reconnection has evolved significantly over the history of plasma physics. The classical Sweet-Parker model of reconnection uses dimensional arguments to infer parameters such as the width of a long, thin, steady-state current sheet. Its fundamental prediction is that the current sheet width is $\delta_{\mathrm{SP}} = LS^{-1/2}$, where L is its length and $S = \mu_0 L v_A/\eta$ is the Lundquist number [12,13], with v_A the Alfvén velocity computed with the reconnecting field and η is the plasma resistivity. Consequently, the Sweet-Parker reconnection timescale is $\tau_{\mathrm{SP}} \sim S^{1/2}L/v_A$. Since typical reconnecting plasmas have $S \gg 1$ as a result of very small resistivity, the Sweet-Parker timescale is orders of magnitude too large to explain observations of reconnection in astrophysical and laboratory contexts.

Modern reconnection theories and associated simulations [14–20] improve upon the Sweet-Parker model by revealing the vulnerability of long, thin current sheets to the plasmoid instability. This leads to the formation of chains of magnetic islands, known as "plasmoids," which enhance the reconnection rate and associated dissipation of magnetic energy by eliminating the dependence of the reconnection rate on the global Lundquist number of the current sheet [17,20]. Plasmoids are thought to be a generic feature of large-scale reconnecting systems, having been observed in a wide range of parameter regimes.

To date, most magnetic reconnection experiments performed to seek out observations of plasmoids have investigated two regimes: relatively tenuous quasi-steady-state magnetically driven plasmas for which the typical plasma β (the ratio of thermal pressure to magnetic pressure) is $\beta \ll 1$ [7,8]; and pulsed-power driven plasmas for which $\beta \lesssim 1$ [9,21]. In magnetically driven experiments, plasma inflows remain sub-Alfvénic; in pulsed-power driven systems, super-Alfvénic flows and associated flux pileup were observed [21].

We report here the direct observation of plasmoids in a laser-driven reconnection experiment with high plasma β ($\sim$10) and super-Alfvénic inflows, using modern proton radiography and deflection-field reconstruction techniques [22,23] which allow unprecedented insight into the structure of magnetic fields in high-energy-density physics experiments, alongside time-resolved Thomson scattering to characterize important plasma parameters [24]. While previous laser-driven experiments have been performed to investigate magnetic reconnection (e.g., [25]), prior campaigns have not directly observed plasmoid formation; in contrast our results show strong direct evidence of plasmoids. The conditions in our experiment manifest experimental regimes which are typical of laser-produced plasmas in laboratory experiments [10,11,26], and which match certain parameters of astrophysical plasmas, such as the high-β plasmas of the intracluster medium [27,28] or the Galactic center [29].

Our laser-produced plasma magnetic reconnection experiment was carried out at the OMEGA EP laser facility [30]. Initial findings on a subset of the data were reported by Rosenberg *et al.* [31]. In this study, we use modern,

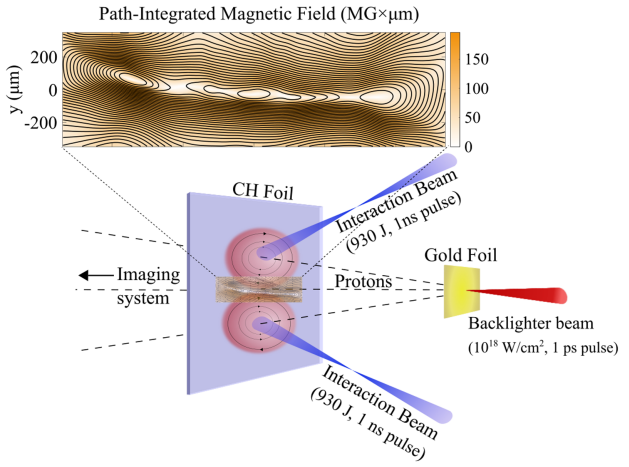

FIG. 1. Experimental design. A plastic (CH) foil illuminated by two interaction laser beams, producing plasma bubbles. A proton backlighter consisting of a gold foil driven by a high-power, short-pulse laser beam produces energetic protons, which generate proton images after passing through the subject configuration. The collision between two antiparallel magnetic fields driven by the bubble expansion leads to the changing of the field topology and reconnection, as indicated in the reconstructed fields shown in the inset.

TABLE I. Quantities relevant to discussions of this experiment. Those above the horizontal line are extracted from either radiography or Thomson scattering data; quantities below the horizontal line are calculated based on those measurements. The "magnetic field" quantity is obtained by assuming a path length traversed by backlighting protons then calculated based on the reconstructed path-integrated values.

Parameter	Approximate value
Plasma density, n_e	3.2×10^{19} cm^{-3}
Electron temperature, T_e	2.2 keV
Magnetic field (near CS), B	40–70 T
Length of current sheet, L	~2000 μm
Width of current sheet, δ	20–60 μm
Plasma beta, β	~10
Ion skin depth, d_i	~55 μm
Electron skin depth, d_e	~1 μm
Spitzer resistivity, η	$\sim 4 \times 10^{-2}$ Ω μm
Sound speed, c_s	$\sim 4.69 \times 10^{11}$ μm/s
Alfvén speed, v_A	$\sim 1.5 \times 10^{11}$ μm/s
Lundquist number, S	~9000–15000
CS width/ion scale, δ/d_i	~0.2–1

sophisticated analysis techniques not available at the time of publication of [31] and which enable much more detailed investigation of the magnetic field structure, to analyze the remainder of the large data set from the shot day. In addition, to characterize plasma parameters an experiment with nominally identical drive conditions was carried out at the OMEGA Laser Facility in 2019 to perform Thomson scattering measurements.

The experimental setup is shown schematically in Fig. 1. In the experiment, the subject target is a 12 μm thick plastic (CH) foil, driven by two 1-ns square pulse interaction beams of 930 J each, with spot sizes of 800 μm and a separation of 1400 μm. The interaction beams impinging on the CH foil produced two hemispherical plasma bubbles. The Thomson scattering measurements indicate that such bubbles have a typical plasma temperature $T_e \sim 2$ keV, electron density $n_e \sim 3 \times 10^{19}$ cm^{-3}, and bubble expansion velocity $v \sim 500$–800 μm/ns immediately prior to collision (see Table I); the results of this analysis are roughly consistent with DRACO simulations of the experiment [31].

The bubbles produced circulating magnetic fields via the Biermann battery mechanism [32], wherein a magnetic field is generated due to misaligned temperature and density gradients: $\partial_t \vec{B} \propto \nabla T_e \times \nabla n_e$. As illustrated in Fig. 1, the two plasma bubbles expand into each other, compressing their antiparallel magnetic fields and driving the reconnection process.

Figure 2 presents the proton fluence radiographs of the reconnecting plasma bubbles, imaged with ~10–40 MeV protons generated simultaneously at the gold foil

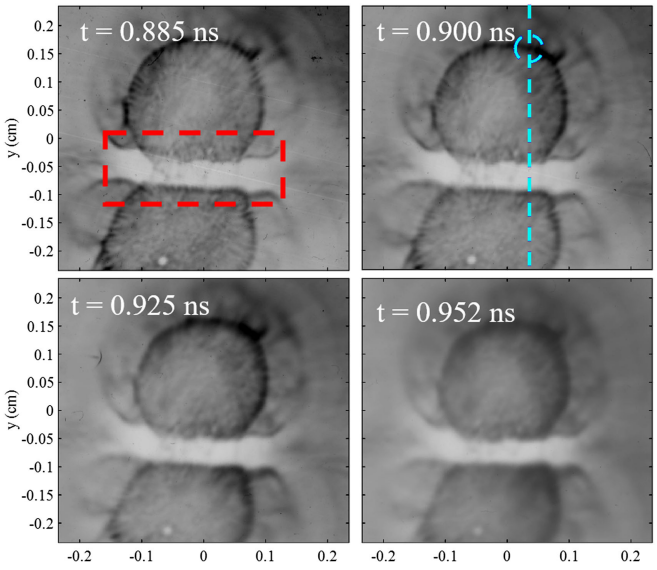

FIG. 2. Raw radiography data. Proton radiographs show the spatial structure and temporal evolution of magnetic fields associated with the expanding plasma bubbles and interaction regions. These radiographs were formed by protons with energies between 11 and 36 MeV. The dashed cyan line in the second image represents approximately where lineouts for Figs. 5(a) and 5(b) were taken, though each image had a slightly different location for the lineout to ensure sampling of the correct current sheet structure (between apparent plasmoids). The dashed cyan circle denotes the position of edge of the Biermann bubble along the lineout. In these images, image contrast has been artificially increased to render the structure in the center of the radiograph more visible to the naked eye.

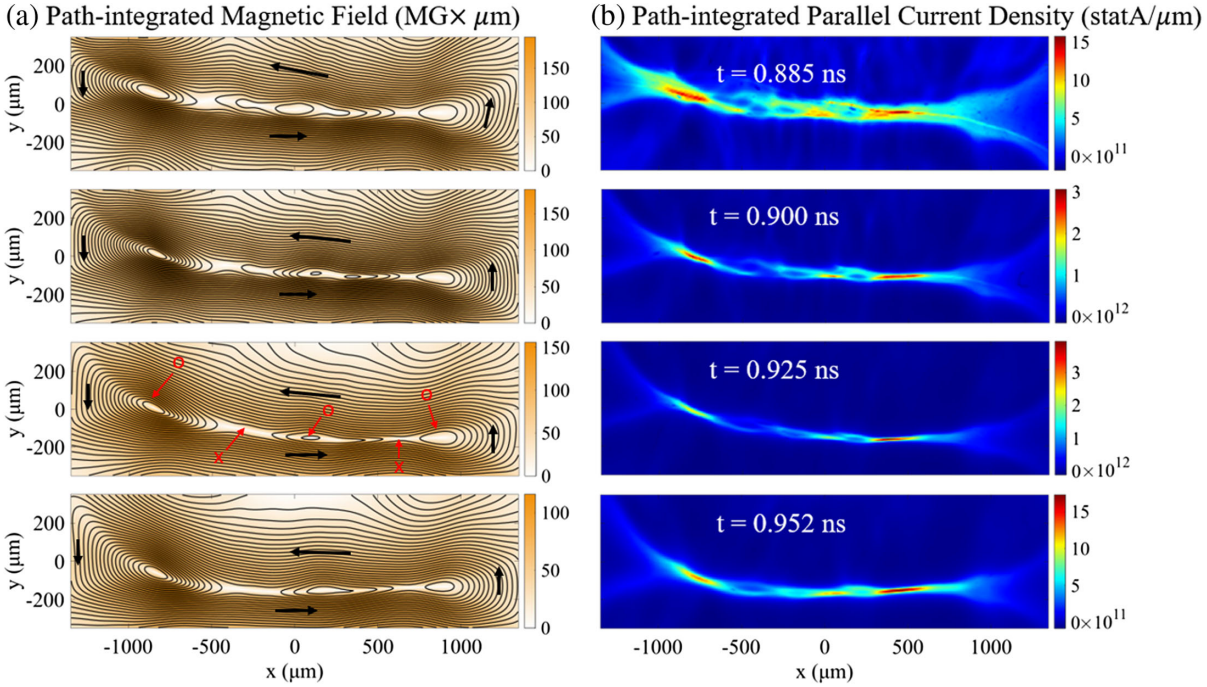

FIG. 3. Reconstructed path-integrated fields and currents. (a) The reconstructed magnetic fields from the radiography data. All of these reconstructions are of different films from the same experimental shot. The black curves in the magnetic field strength plots denote contours of the path-integrated magnetic vector potential $\vec{A}$, while the black arrows denote the approximate direction of the magnetic field at their locations. The presence of isolated magnetic islands is evident in all of the radiographs. The third panel in this column additionally has labeled O and X points in the magnetic field topology, corresponding to the lineout in Fig. 4. (b) The inferred path-integrated parallel current, obtained from Ampére's law by taking the curl of the path-integrated magnetic field: $\nabla \times \vec{B}_p = \mu_0 \vec{j}_p$, where the p subscript denotes a path-integrated quantity.

(positioned 8 mm in front of the experimental configuration) by a high-power short pulse laser based on the target-normal-sheath-acceleration (TNSA) mechanism [33]. These protons are deposited on a stack of radiochromic film positioned 120 mm behind the experimental configuration.

The concentration of proton fluence in a circular pattern around each bubble is the consequence of inward proton deflections caused by large scale, azimuthal Biermann fields. Between the two expanding plasma bubbles, the pale central region with a noticeable deficit of proton fluence represents a reconnection layer with a large length L to apparent width δ aspect ratio. To quantitatively characterize the field distribution associated with the reconnection layer, the measured radiographs are numerically reconstructed with a finite-difference Monge-Ampére solving algorithm [23]. Details about the assumptions and approximations made in reconstructing the data (which are standard in radiography reconstruction) are included in the Appendix.

Figure 3(a) shows the path-integrated magnetic field strength inferred from the deflection-field reconstruction process in the reconnection region overlaid with contours of the path-integrated magnetic vector potential. The reconnection region is approximately delineated by the dashed red box in the first image of Fig. 2. The magnetic field strength increases to a peak off-center of the reconnection layer before decreasing and rapidly switching direction as the center is crossed. This observation matches the intuitive form of the magnetic field one would infer based on the radiography data: the large white region with low proton flux implies the presence of strong fields, while the dark regions on either side indicate that the field points in opposite directions on either side of the center.

More notably, Fig. 3(a) clearly reveals the presence of striking, isolated magnetic islands in the reconnection layer, which are clearly identifiable by the appearance of closed magnetic field lines. This identification is strongly justified considering the high spatial resolution of the proton radiography (~5 μm). We are able to well resolve the measured plasmoid structure [for example, the width of a primary plasmoid is ~100–200 μm, Fig. 3(a)], thus providing strong experimental evidence of plasmoid formation in this high-β reconnection event.

Several important features related to the time evolution of the reconnection layer and its constituent plasmoids are visible in Fig. 3(a). First, from 0.885 to 0.952 ns we see that the leftmost plasmoid appears to continuously grow in both area and width, although as we discuss later this is unlikely to be a reconnection effect. Meanwhile, there are suggestions in the central region of smaller, second-generation

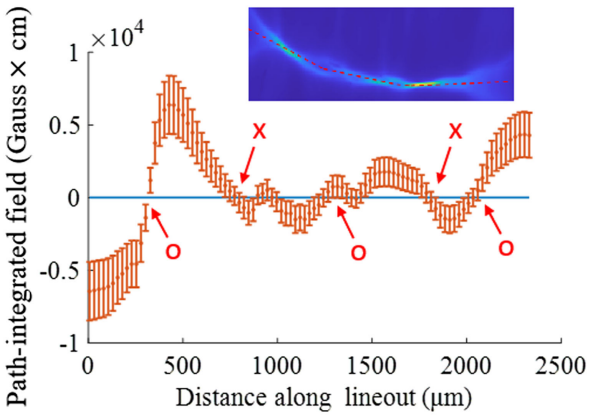

FIG. 4. Lineout along the current sheet. The lineout of the vertical path-integrated magnetic field along the direction of the current sheet, with error bars indicating the approximate uncertainty in the path-integrated field information. The labeled X and O points on the plot correspond to those labeled on the third panel of Fig. 3(a). The data here have been spatially down sampled for visual clarity, so the placement of individual data points does not correspond to the spatial resolution of the system. The inset at top right is a reproduction of the path-integrated parallel current from the third panel Fig. 3(b) showing where the lineout along the current sheet is located.

("secondary") plasmoids with apparent widths above our predicted spatial resolution of ~5 μm, though we consider this identification marginal.

The inferred path-integrated current density parallel to the direction of proton propagation (calculated directly from the path-integrated fields by using Ampére's law) is displayed in Fig. 3(b), from which we measure a current sheet length $L \sim 2000$ μm (indicating that $L/d_i \sim 35$, where $d_i = c/\omega_{pi}$ is the ion skin depth). It is clear from these images that the current sheet is not laminar or uniform, and instead is highly dynamic. One way this manifests is in the transition from an initially rather broad current sheet (at $t = 0.884$ ns) to a much narrower current sheet at later times.

Figure 4 shows a lineout of the vertical magnetic field along the direction of the current sheet, with associated inferred uncertainty in the path-integrated field indicated by the vertical error bars (the physical location of the lineout relative to the current sheet is shown in the inset at top right). The uncertainty in the path-integrated field is assessed by varying inferred reconstructed path-integrated fields, then using the modified fields to produce synthetic proton images. Variation outside of the range indicated on Fig. 4 yields a poor match between the synthetic and measured proton images. Places where the sign of the vertical field changes unambiguously correspond to X and O points in the magnetic field topology. Five such points are present, corresponding to three O points and two X points, consistent with the field topology shown in the third panel of Fig. 3(a). Additional candidate locations where the measured field appears to change direction, but not outside the error limits, correspond to the marginal second-generation plasmoids previously referenced.

Our interpretation of these data is that as the two Biermann bubbles expand into each other, an extended current sheet is formed whose aspect ratio L/δ increases as a function of time at supersonic rates. This implies that the current sheet becomes progressively more unstable to the tearing instability [34,35], resulting in the onset of plasmoid formation while the width of the current sheet δ is still above the ion kinetic scale d_i. Subsequently, the sheet narrows to widths below d_i suggesting that ion kinetic effects become important, but remains well separated from the electron kinetic scale $d_e \sim 1$ μm, which is the expected characteristic thickness if the frozen flux condition were broken by electron inertia. This suggests that the reconnection is instead mediated by resistivity, and that reconnection is occurring in the Hall MHD regime during these observations of the CS.

We note that quantitative comparison to existing reconnection theory is difficult; the experiment's evolving current sheet (the evolution sampled here occurs on a timescale roughly 10 times faster than the Alfvèn transit time) with strongly driven inflows is a large departure from the steady-state Sweet-Parker-type background considered in analyses of reconnection in similar parameter regimes (such as [36]).

In the subsequent evolution of the current sheet, we observe further shrinkage of its width to below the ion skin depth, as shown in Fig. 6(a), due to the continued expansion of the Biermann bubbles ($v \sim 800$ μm/ns, faster than reconnection timescales) over the course of the experiment.

This narrowing effect of the current sheet is explored more fully in Fig. 5, showing lineouts of the path-integrated magnetic field [Fig. 5(a)] and lineouts of the path-integrated current density [Fig. 5(b)] at each time step [lineouts of Figs. 3(a) and 3(b), respectively]. The variations in magnetic field shown in Fig. 5(a) give important insight into the reconnection process; the most dramatic observation is an increase in magnetic field strength near the current sheet, when compared with the outer edge of a bubble, providing experimental evidence of the magnetic flux pileup which is expected given super Alfvénic inflows. From Fig. 5(b), we can infer the width of the current sheet δ by measuring the full width at half-maximum of the path-integrated current peaks [shown in Fig. 5(a) and discussed below].

Figure 6(a) displays the time evolution of the current sheet width through X points in the current sheet (these are the widths inferred from Fig. 5(b), with the right-hand axis showing the ratio of the width to the ion skin depth. We see that at the earliest time the current sheet is wider than the ion skin depth, but subsequently narrows to below the ion scale as the two plasma bubbles continue to expand into each other.

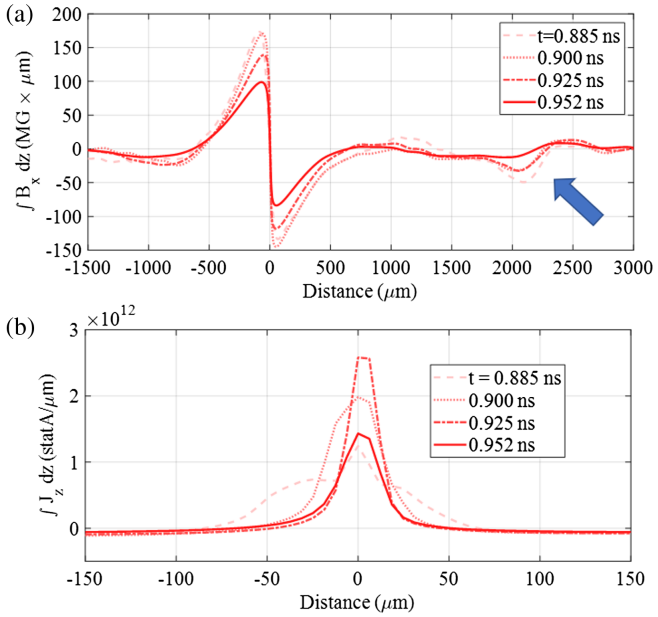

FIG. 5. Lineouts through the current sheet. (a) Lineouts of the path-integrated x-directed magnetic field at each time step, showing the piling up of magnetic flux on either side of the reconnection layer. The blue arrow denotes the approximate location of the edge of a Biermann bubble (referred to later as "far from the current sheet"), demonstrating that the field strength is considerably higher in the reconnection layer than outside of it. (b) Lineouts of the path integrated parallel current at each time step (enlarged to show detail—note restricted horizontal length scale).

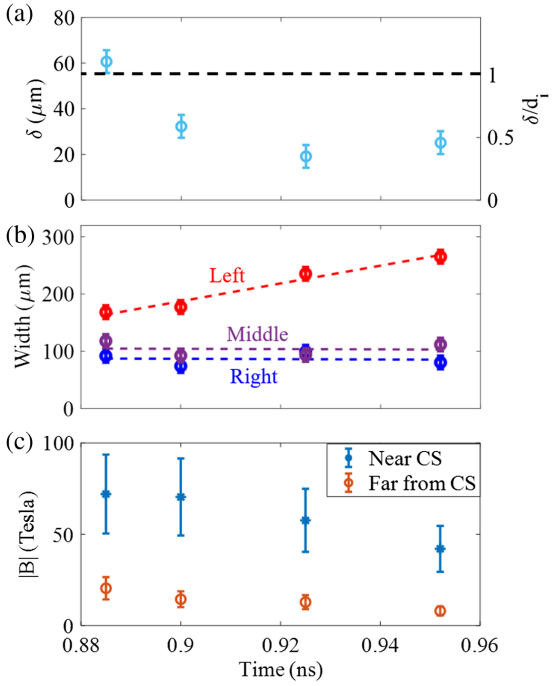

FIG. 6. Time evolution of various quantities. (a) The width of the current sheet, inferred from the lineouts in Fig. 5, over time. The left axis shows the width in microns, while the right axis shows the ratio of the measured width to the calculated ion skin depth. (b) The measured width of the various plasmoids, perpendicular to the "horizontal" direction of the current sheet, as inferred from the largest closed contours of the path-integrated magnetic vector potential (located by selecting the potential at an adjacent X point). (c) The peak magnetic field near the center of the current sheet plotted alongside the representative magnetic field near the edge of an expanding bubble ["far from CS," see Figs. 2 and 5(a)].

Shown in Fig. 6(b) is the time evolution of the width of the three large plasmoids observed in the experiment. The central and rightmost plasmoids display no increase in width over the experimental timescale, within error bar. This is consistent with theoretical expectations; assuming a nominal reconnection rate of $\sim 0.1 v_A$ (consistent with ion kinetic effects being important), the anticipated increase in plasmoid width is on the order of a few microns, below our experimental resolution. Conversely, the leftmost plasmoid displays an apparent rapid growth that cannot be explained by timescales associated with the reconnection theory. Geometrical effects caused by the finite size of the experimental region could explain this observation; significant edge effects caused by the flows of the expanding Biermann bubbles could lead to this anomalous growth. Because the bubbles are nearly circular, the region where they collide and interact is not completely uniform, and instead has a smaller region of uniformity flanked by areas where edge effects may be significant. An asymmetry in the flows driving the expansion of one bubble could then contribute to the anomalous growth of the leftmost island. A comparison of the apparent width growth rate (~1300 μm/ns) to the bubble expansion velocity (~800 μm/ns from each side) suggests that this explanation is reasonable.

Meanwhile, Fig. 6(c) measures the magnitude flux pileup effects over the timescale of the experiment. We observe that the strength of the magnetic field in a region on the far sides of the expanding plasma bubbles is consistently lower than the strength of the magnetic field in the interior region of the current sheet by a factor which varies between 3 and 6.

This work represents a significant step forward in the understanding of high-β magnetic reconnection. One aspect we wish to emphasize is the value of this diagnostic suite in experiments of this type, namely the application of the radiography reconstruction routine to TNSA proton radiographs. Often, laser experiments which utilize proton radiography use a monoenergetic, imploding capsule-type backlighter (for example, [26]); in such an experiment, the spatial resolution of the proton radiography (and therefore the structure of the reconstructed fields and currents) is inherently limited by the finite size of the backlighter. TNSA radiography has the significant advantage of a considerably smaller proton source size. By combining the TNSA radiography with the reconstruction algorithm,

we are able to utilize both to their fullest potential to examine the evolution of the experiment on both rapid timescales and small spatial scales.

In summary, these experiments provide direct experimental evidence of plasmoid formation in high-β magnetic reconnection. Modern theories [17] and understanding of magnetic reconnection hinge on the instability of thin current sheets leading to the formation of plasmoids and enhancement of the reconnection rate. Recent work on plasmoid formation in weakly collisional plasmas due to the mirror instability [37] may describe the conditions present in this experiment. Such results coupled with observations like ours indicate that an understanding of plasmoid-mediated reconnection can be applied to a wider set of parameter regimes than those in which plasmoids have been observed in the past.

Additionally, we anticipate that the diagnostic suite utilized in this experiment can be fruitfully applied to investigate phenomena related to the evolution of reconnecting current sheets, such as the onset of plasmoid formation very early in the CS lifetime, or late-time evolution (merging, coalescence, and eventual ejection) of plasmoids in the CS; other experimental searches along these lines in related parameter spaces are already bearing fruit [38]. In these ways, this experiment helps pave the way for a a deeper understanding of magnetic reconnection in laboratory and astrophysical plasmas.

This work was supported in part by U.S. DOE/NNSA CoE Contract No. DE-NA0003868, U.S. DoE/NNSA Award No. DE-NA0003856, DOE/NNSA HEDLP Contract No. DE-NA0004129, NLUF Contract No. DE-NA0003938, U.S. DOE (Grants No. DE-FG03-09NA29553, No. DE-SC0007168), LLE (No. 414090-G), NSF-DOE Partnership in Basic Plasma Science and Engineering Award No. PHY-2010136, and joint NSF/DOE-NNSA Award No. PHY2108050.

Appendix: Methods.—The temporal resolution of the radiography is a result of time-of-flight differences between protons of varying energies. Differential filtration of the film packs leads to each film in the stack being sensitive to a different proton energy; then protons with these differing energies have different times of flight from the gold foil, allowing probing of the reconnection region at different times. In our analysis, we have assumed that the bulk of the structure of each radiograph is determined by particles carrying energy near the Bragg peak, where the sensitivity is highest, though there is also some (exponentially suppressed) contribution from higher-energy particles on each film [22], resulting in a "blurring" or "smearing" of the primary structure. So long as we choose films which have sufficiently high proton flux and minimal blurring, the monoenergetic assumption is unlikely to introduce significant uncertainty in the analysis.

Characterization of the initial proton flux prior to interaction with magnetic fields is important in the reconstruction procedure. In a typical null shot, we observe low-amplitude large-scale spatial variations of the order of the image size, but no high-frequency nonuniformities that could be confused with physics effects seen in the reconstructions. This suggests that it is reasonable to infer initial proton fluxes by filtering out high-frequency nonuniformities in the flux images while keeping total proton flux constant, as previous authors have done [23].

In addition to the previously noted inferences made about the proton flux images, usage of the reconstruction algorithm also assumes that proton tracks do not cross each other between the source and the detector screen (i.e., that the relationship between initial proton trajectories and their final positions on the screen is injective). Additionally, we assume that magnetic fields are the dominant factor causing proton deflections in the face-on radiography, as has been experimentally validated [39]. Once these assumptions are made, the reconstruction can be carried out.

One other point which is important to remember is that all of these results are an interpretation of path-integrated fields, which are necessarily integrated along the direction of proton propagation. If the current sheet layer has significant 3D structure along this direction, these results may have additional complications which need to be considered during analysis. Because of experimental constraints, we were not able to perform simultaneous side-on imaging of this experiment; thus, variation along the probing direction cannot be ruled out, and the possibility of such effects must be kept in mind when assessing these results. We also wish to note here that in these discussions the ions have been simply treated approximately as a single species by averaging the hydrogen and carbon (in a 1:1 ratio, and fully ionized). Quantitatively addressing the details of spatial structure and dynamics and species separation associated with a two-ion fluid plasma is a significant challenge for future work.

*pearcy@mit.edu
†ckli@mit.edu

[1] D. Biskamp, *Magnetic Reconnection in Plasmas* (Cambridge University Press, Cambridge, England, 2000).
[2] M. Yamada, R. Kulsrud, and H. Ji, Magnetic reconnection, Rev. Mod. Phys. **82**, 603 (2010).
[3] E. G. Zweibel and M. Yamada, Magnetic reconnection in astrophysical and laboratory plasmas, Annu. Rev. Astron. Astrophys. **47**, 291 (2009).
[4] S. Masuda, T. Kosugi, H. Hara, S. Tsuneta, and Y. Ogawara, A loop-top hard x-ray source in a compact solar flare as evidence for magnetic reconnection, Nature (London) **371**, 495 (1994).
[5] T. D. Phan, J. T. Gosling, M. S. Davis *et al.*, A magnetic reconnection x-line extending more than 390 Earth radii in the solar wind, Nature (London) **439**, 175 (2006).

[6] J. B. Taylor, Relaxation and magnetic reconnection in plasmas, Rev. Mod. Phys. **58**, 741 (1986).

[7] J. Olson, J. Egedal, S. Greess *et al.*, Experimental demonstration of the collisionless plasmoid instability below the ion kinetic scale during magnetic reconnection, Phys. Rev. Lett. **116**, 255001 (2016).

[8] J. Jara-Almonte, H. Ji, M. Yamada, J. Yoo, and W. Fox, Laboratory observation of resistive electron tearing in a two-fluid reconnecting current sheet, Phys. Rev. Lett. **117**, 095001 (2016).

[9] J. Hare, L. Suttle, S. Lebedev *et al.*, Anomalous heating and plasmoid formation in a driven magnetic reconnection experiment, Phys. Rev. Lett. **118**, 085001 (2017).

[10] P. M. Nilson, L. Willingale, M. C. Kaluza *et al.*, Magnetic reconnection and plasma dynamics in two-beam laser-solid interactions, Phys. Rev. Lett. **97**, 255001 (2006).

[11] C. K. Li, F. H. Séguin, J. A. Frenje, J. R. Rygg, R. D. Petrasso, R. P. J. Town, O. L. Landen, J. P. Knauer, and V. A. Smalyuk, Observation of megagauss-field topology changes due to magnetic reconnection in laser-produced plasmas, Phys. Rev. Lett. **99**, 055001 (2007).

[12] B. Lehnert, *Electromagnetic Phenomena in Cosmical Physics* (Cambridge University Press, Cambridge, 2016).

[13] E. N. Parker, Sweet's mechanism for merging magnetic fields in conducting fluids, J. Geophys. Res. **62**, 509 (1957).

[14] N. F. Loureiro, A. A. Schekochihin, and S. C. Cowley, Instability of current sheets and formation of plasmoid chains, Phys. Plasmas **14**, 100703 (2007).

[15] A. Bhattacharjee, Y.-M. Huang, H. Yang, and B. Rogers, Fast reconnection in high-Lundquist-number plasmas due to the plasmoid instability, Phys. Plasmas **16**, 112102 (2009).

[16] W. Daughton, V. Roytershteyn, B. J. Albright, H. Karimabadi, L. Yin, and K. J. Bowers, Transition from collisional to kinetic regimes in large-scale reconnection layers, Phys. Rev. Lett. **103**, 065004 (2009).

[17] N. F. Loureiro and D. A. Uzdensky, Magnetic reconnection: From the Sweet-Parker model to stochastic plasmoid chains, Plasma Phys. Controlled Fusion **58**, 014021 (2016).

[18] S. D. Baalrud, A. Bhattacharjee, Y.-M. Huang, and K. Germaschewski, Hall magnetohydrodynamic reconnection in the plasmoid unstable regime, Phys. Plasmas **18**, 092108 (2011).

[19] H. Ji and W. Daughton, Phase diagram for magnetic reconnection in heliophysical, astrophysical, and laboratory plasmas, Phys. Plasmas **18**, 111207 (2011).

[20] D. A. Uzdensky, N. F. Loureiro, and A. A. Schekochihin, Fast magnetic reconnection in the plasmoid-dominated regime, Phys. Rev. Lett. **105**, 235002 (2010).

[21] J. D. Hare, L. G. Suttle, S. V. Lebedev *et al.*, An experimental platform for pulsed-power driven magnetic reconnection, Phys. Plasmas **25**, 055703 (2018).

[22] A. B. Zylstra, C. K. Li, H. G. Rinderknecht *et al.*, Using high-intensity laser-generated energetic protons to radiograph directly driven implosions, Rev. Sci. Instrum. **83**, 013511 (2012).

[23] A. F. A. Bott, C. Graziani, P. Tzeferacos, T. G. White, D. Q. Lamb, G. Gregori, and A. A. Schekochihin, Proton imaging of stochastic magnetic fields, J. Plasma Phys. **83**, 905830614 (2017).

[24] *Plasma Scattering of Electromagnetic Radiation: Experiment, Theory and Computation*, 1st ed., edited by D. Froula (Elsevier, Amsterdam, Boston, 2011).

[25] W. Fox, D. B. Schaeffer, M. J. Rosenberg *et al.*, Fast magnetic reconnection in highly-extended current sheets at the National Ignition Facility, arXiv:2003.06351.

[26] M. Rosenberg, C. K. Li, W. Fox, I. Igumenshchev, F. H. Séguin, R. P. J. Town, J. A. Frenje, C. Stoeckl, V. Glebov, and R. D. Petrasso, A laboratory study of asymmetric magnetic reconnection in strongly driven plasmas, Nat. Commun. **6**, 6190 (2015).

[27] C. L. Carilli and G. B. Taylor, Cluster magnetic fields, Annu. Rev. Astron. Astrophys. **40**, 319 (2002).

[28] F. Govoni, M. Murgia, V. Vacca *et al.*, Sardinia radio telescope observations of Abell 194: The intra-cluster magnetic field power spectrum, Astron. Astrophys. **603**, A122 (2017).

[29] A. Alt and M. W. Kunz, Onset of magnetic reconnection in a collisionless, high-β plasma, J. Plasma Phys. **85**, 175850102 (2019).

[30] L. Waxer, D. Maywar, J. Kelly *et al.*, High-energy petawatt capability for the omega laser, Opt. Photonics News **16**, 30 (2005).

[31] M. Rosenberg, C. K. Li, W. Fox, A. B. Zylstra, C. Stoeckl, F. H. Séguin, J. A. Frenje, and R. D. Petrasso, Slowing of magnetic reconnection concurrent with weakening plasma inflows and increasing collisionality in strongly driven laser-plasma experiments, Phys. Rev. Lett. **114**, 205004 (2015).

[32] L. Biermann, Über den Ursprung der Magnetfelder auf Sternen und im interstellaren Raum (miteinem Anhang von A. Schlüter), Z. Naturforsch. A **5**, 65 (1950).

[33] S. P. Hatchett, C. G. Brown, T. E. Cowan *et al.*, Electron, photon, and ion beams from the relativistic interaction of petawatt laser pulses with solid targets, Phys. Plasmas **7**, 2076 (2000).

[34] D. A. Uzdensky and N. F. Loureiro, Magnetic reconnection onset via disruption of a forming current sheet by the tearing instability, Phys. Rev. Lett. **116**, 105003 (2016).

[35] E. A. Tolman, N. F. Loureiro, and D. A. Uzdensky, Development of tearing instability in a current sheet forming by sheared incompressible flow, J. Plasma Phys. **84**, 905840115 (2018).

[36] P. Bhat and N. F. Loureiro, Plasmoid instability in the semi-collisional regime, J. Plasma Phys. **84**, 905840607 (2018).

[37] H. W. Winarto and M. W. Kunz, Triggering tearing in a forming current sheet with the mirror instability, J. Plasma Phys. **88**, 905880210 (2022).

[38] Z. Zhao, H. An, Y. Xie, Z. Lei, W. Yao, W. Yuan, J. Xiong, C. Wang, J. Ye, Z. Xie, Z. Fang, A. Lei, W. Pei, X. He, W. Zhou, W. Wang, S. Zhu, and B. Qiao, Laboratory observation of plasmoid-dominated magnetic reconnection in hybrid collisional-collisionless regime, Commun. Phys. **5**, 247 (2022).

[39] C. K. Li, F. H. Séguin, J. A. Frenje *et al.*, Measuring E and B fields in laser-produced plasmas with monoenergetic proton radiography, Phys. Rev. Lett. **97**, 135003 (2006).